

Constraints on UV Absorption in the Intracluster Medium of Abell 1030¹

Anton M. Koekemoer, Christopher P. O’Dea, Stefi A. Baum

Space Telescope Science Institute, 3700 San Martin Drive, Baltimore, MD 21218; koekemoer@stsci.edu, odea@stsci.edu, sbaum@stsci.edu

Craig L. Sarazin

Department of Astronomy, University of Virginia, P.O. Box 3818, Charlottesville, VA 22903-0818; cls7i@coma.astro.virginia.edu

Frazer N. Owen

National Radio Astronomy Observatory,² P.O. Box 0, Socorro, NM 87801; fowen@aoc.nrao.edu

Michael J. Ledlow³

Department of Astronomy, New Mexico State University, Las Cruces, NM 88003; mledlow@astro.phys.unm.edu

Submitted to *The Astrophysical Journal*

Received 1997 October 30; accepted 1998 June 29

ABSTRACT

We present results from an extensive HST spectroscopic search for UV absorption lines in the spectrum of the quasar B2 1028+313, which is associated with the central dominant galaxy in the cluster Abell 1030 ($z = 0.178$). This is one of the brightest known UV continuum sources located in a cluster, and therefore provides an ideal opportunity to obtain stringent constraints on the column densities of any cool absorbing gas that may be associated with the intracluster medium (ICM). Our HST spectra were obtained with the FOS and GHRS, and provide continuous coverage at rest-frame wavelengths from ~ 975 to 4060 \AA , thereby allowing the investigation of many different elements and ionization levels. We utilize a new technique that involves simultaneous fitting of large numbers of different transitions for each species, thereby yielding more robust constraints on column densities than can be obtained from a single transition. This method yields upper limits of $\lesssim 10^{11} - 10^{13} \text{ cm}^{-2}$ on the column densities of a wide range of molecular, atomic and ionized species that may be associated with the ICM. We also discuss a possible Ly α and C IV absorption system associated with the quasar. We discuss the implications of the upper limits on cool intracluster gas in the context of the physical properties of the ICM and its relationship to the quasar.

Subject headings: intergalactic medium — quasars: absorption lines — galaxies: clusters: individual (A1030) — ultraviolet: galaxies

¹Based on observations made with the NASA/ESA Hubble Space Telescope, obtained at the Space Telescope Science Institute, which is operated by the Association of Universities for Research in Astronomy, Inc., under NASA contract NAS 5-26555.

²The National Radio Astronomy Observatory is operated by Associated Universities, Inc., under contract with the National Science Foundation.

³Current address: Department of Physics and Astronomy, Institute for Astrophysics, University of New Mexico, Albuquerque, NM 87131

1. Introduction

Clusters of galaxies generally display diffuse X-ray emission at keV energies, spatially extended on scales up to several Mpc. This radiation is a consequence of thermal bremsstrahlung from the hot, diffuse intracluster medium (ICM) associated with the cluster, which is typically found to have temperatures $T \sim 10^7 - 10^8$ K and densities $n \sim 10^{-2} - 10^{-4}$ cm $^{-3}$ (e.g., Sarazin 1986). A fundamental question in the study of ICM physics concerns the amount of cooler material, if any, that may be present in the ICM, and the physical processes that would correspond to sinks or sources of such cool gas. Such processes include removal of gas from galaxies through ram-pressure stripping or collisions, ejection of material into the ICM from star formation and galaxy activity, accretion of primordial clouds and proto-galaxies by the cluster, and large-scale ICM cooling flows and / or heating processes (Cowie & Binney 1977; Fabian, Nulsen, & Canizares 1991; Soker, Bregman, & Sarazin 1991; Fabian 1994; Rephaeli & Silk 1995).

There have been unsuccessful searches by several groups for direct evidence of cooler atomic and molecular gas that may be generally distributed throughout the ICM (McNamara, Bregman, & O’Connell 1990; Jaffe 1991; Antonucci & Barvainis 1994; Braine & Dupraz 1994; Dwarakanath et al. 1994; O’Dea et al. 1994; O’Dea, Gallimore, & Baum 1995; O’Dea, Payne, & Kocevski 1998). Upper limits are typically in the range $N(\text{H}_2) \lesssim 10^{20}$ cm $^{-2}$, $N(\text{H I}) \lesssim 10^{18}$ cm $^{-2}$, and $M(\text{H}_2 + \text{H I}) \lesssim 10^9 M_\odot$ (O’Dea & Baum 1997), and generally apply to the central ~ 100 kpc of clusters. Some indirect evidence for the presence of cool gas in the ICM has been inferred in a few clusters based on possible detections of far-IR emission from dust (Maoz 1995; Cox, Bregman, & Schombert 1995; Stickel et al. 1998) — the short sputtering times of dust in hot gas would require shielding by atomic / molecular gas in order for it to survive (Dwek, Rephaeli, & Mather 1990; Hu 1992; Voit & Donahue 1995; Braine et al. 1995). However, in these clusters no direct evidence of cool gas (e.g., optical / UV absorption lines) has yet been detected. In a small number of other clusters, atomic / molecular gas has indeed been observed (e.g., Lazareff et al. 1989; O’Dea, Baum, & Gallimore 1994; Jaffe & Bremer 1997), but in each case it appears to be directly associated with the central cluster galaxy and not generally distributed throughout the ICM.

One locus of parameter space where cooler gas phases have been observed for many years is in the central regions ($r \lesssim 10 - 100$ kpc) of cooling flow clusters (e.g., Fabian 1984, 1994; Edge et al. 1992), where the ICM densities and pressures are sufficiently high that cooling should occur on timescales much shorter than the cluster lifetime. Large amounts of cold gas have been inferred from detections of excess soft X-ray absorption towards some of these clusters (White et al. 1991; Allen et al. 1993). Optical emission lines from $\sim 10^4$ K gas are also seen in their central regions (e.g., Donahue & Voit 1997), together with direct evidence of dust (e.g., Hu 1992; McNamara et al. 1996) and atomic and molecular gas (O’Dea & Baum 1997). However, the amounts of colder gas detected in the optical or radio are too small to account for the total mass expected to have cooled over a Hubble time, and are also incompatible with the high X-ray absorption column densities.

Thus, very little is known about the possible existence, total amount, and physical state of cooler material in the more diffuse ICM that is found in the majority of clusters, which do not specifically exhibit cooling flows but which nevertheless might possess a cool phase. For example, the extreme UV emission recently detected toward some clusters (Lieu et al. 1996a,b; Mittaz et al. 1997) may indicate the presence of a cooler phase with $T \lesssim 10^6$ K (although another probable origin for this emission may be inverse Compton scattering of cosmic microwave background radiation by cosmic-ray electrons in the ICM; Sarazin & Lieu 1998). UV absorption line studies provide several unique advantages in carrying out independent searches for cooler material. First, they are extremely sensitive; columns of gas as small as $\sim 10^{11} - 10^{12}$ cm $^{-2}$ can be detected. Second, several physical states of gas at temperatures $\lesssim 10^6$ K produce UV absorption line features. These include ionized, atomic, and molecular gas. The presence of dust can also be inferred from UV spectra, both through strong reddening and by the 2200 Å dust feature. Third, if cold material is detected, its physical state can be determined by comparing absorption lines from different ions, atoms, and molecules. Finally, the relatively high spectral resolution available in the UV means that the kinematic properties of any detected cool material can be investigated in detail.

On the other hand, UV absorption studies require that a bright source of UV emission be located behind (at least part of) the intracluster gas. For this purpose, the cluster Abell 1030 is

TABLE 1
HST SPECTROSCOPIC OBSERVATIONS OF ABELL 1030

Date	Spectrograph and Grating	Aperture ^a	Exposure Time (s)	Wavelength Coverage (Å)	Instrumental FWHM (Å)
1996 May 17	GHRG G140L	1''74 (2.0)	4800	1150 – 1436	0.87
1996 May 17	GHRG G140L	1''74 (2.0)	2400	1415 – 1702	0.87
1996 May 17	FOS/RD G270H	0''86 (1.0)	1140	2222 – 3277	2.04
1996 May 17	FOS/RD G400H	0''86 (1.0)	300	3235 – 4781	3.00
1996 May 17	FOS/RD G190H ^b	0''86 (1.0)	2400	1572 – 2312	1.47
1996 Nov 22	FOS/RD G190H	0''86 (1.0)	1640	1572 – 2312	1.47

^aWe denote the apertures by following the same convention as in the HST Data Handbook v.3 Volume II, listing the post-COSTAR aperture size in arcseconds together with the pre-COSTAR aperture designation in parentheses.

^bThis observation produced no usable data, since the FOS aperture door closed during the exposure. It was therefore repeated on 1996 Nov 22.

ideal. The central dominant galaxy of this richness 0 cluster (Abell et al. 1989) contains the UV and X-ray bright quasar B2 1028+313 (Owen et al. 1993, 1996; Owen & Ledlow 1997; Sarazin et al. 1998). Its relative proximity ($z = 0.1782 \pm 0.0002$, Owen et al. 1995) and high UV flux makes it one of the brightest known UV sources located in a cluster of galaxies, therefore ideal for obtaining strong constraints on UV line absorption.

2. Observations

In this paper we present high-resolution ultraviolet spectra of B2 1028+313, obtained during 1996 with the Faint Object Spectrograph (FOS) and the Goddard High-Resolution Spectrograph (GHRG) on board the Hubble Space Telescope (HST). We observed B2 1028+313 with three high-dispersion gratings G190H, G270H, and G400H using the FOS/RD camera, and with the low-dispersion G140L grating on the GHRG using the Digicon-1 detector. Further details of the individual exposures are presented in Table 1. All the FOS observations were taken in the standard 512-diode FOS spectrophotometric observing mode ACCUM, sampling each diode with NXSTEPS = 4 pixels and with a total number of overscan steps set to OVERSCAN = 5. The GHRG spectra were obtained in ACCUM mode with FP-SPLIT=NONE and STEP-PATT = 5, thus sampling each of the 500 science diodes with 4 pixels.

Recalibration of the data was performed using the IRAF/STSDAS⁴ pipeline processing software for the HST/FOS and GHRG instruments, using updated calibration reference files where applicable. Specifically, a substantial amount of effort was spent on ensuring the accuracy of the FOS flat-field corrections, both through the use of new “superflat” FOS calibration spectra and related files created by the FOS science team in 1997, as well as by comparing residuals from calibrations performed with different flat-fields obtained around the same epochs as the observations. The resulting flat-field calibration represents a substantial improvement over the initial HST data calibration products. The absolute zero points of the wavelength scales produced by the calibration software also differ slightly for each of our various FOS and GHRG spectra, owing to a number of fundamental uncertainties in the observations (for example, filter-grating wheel positioning offsets). We have addressed this by placing the spectra onto a common wavelength scale defined such that all the singly ionized, strong Galactic ISM absorption lines have a zero mean redshift (similar to the

⁴The Image Reduction and Analysis Facility (IRAF) is distributed by the National Optical Astronomy Observatories, which is operated by the Association of Universities for Research in Astronomy, Inc., under contract to the National Science Foundation. The Space Telescope Science Data Analysis System (STSDAS) is distributed by the Space Telescope Science Institute.

method employed in the the HST Quasar Absorption Line Key Project, described in Schneider et al. 1993). This technique has the advantage that the effects of net velocity shifts of the Galactic ISM towards A 1030 can be easily applied to our data in future studies if required, although such effects would be well outside the scope of the present paper. The final combined set of observations yields a spectrum with continuous wavelength coverage from $\sim 1150 \text{ \AA} - 4780 \text{ \AA}$.

In Figure 1 we present the calibrated HST data from all the gratings, together with two optical spectra obtained by M. Ledlow at the Apache Point Observatory (APO) (see Ledlow et al. 1996 for details of the APO observations and reduction procedures); these data have not been smoothed or rebinned. We present a composite spectrum of the quasar in Figure 2, in which the HST spectra have been rebinned to dispersions $\sim 4 - 6 \text{ \AA/channel}$, in order to match the ground-based optical spectral resolution and better display the general spectral properties of the quasar. The overall quasar spectrum is similar to those of other low-redshift quasars, displaying the broad permitted emission lines of Ly α , C IV, Mg II and the Balmer series, together with narrow forbidden lines such as [Ne V] $\lambda 3426$, [O II] $\lambda 3727$ and [O III] $\lambda \lambda 4959, 5007$. The spectrum shows a strong upturn in the blue, consistent with the power-law ultraviolet increases generally observed in quasar spectra (e.g., Francis et al. 1991; Zheng et al. 1997). We note the presence of strong geocoronal Ly α emission at $\sim 1212 - 1220 \text{ \AA}$, which together with Galactic Ly α absorption conspire to prevent any reliable measurements of O VI $\lambda \lambda 1032, 1038$ absorption at the redshift of Abell 1030.

We used the IRAF/STSDAS 1DFIT package to fit the unabsorbed background “continuum” (thus including the broad quasar emission lines) using a series of spline curves, following similar procedures to those outlined for the HST Quasar Absorption Line Key Project (e.g., Bahcall et al. 1993a; Schneider et al. 1993). The resulting continuum fits are shown in Figure 1a, overlaid on the HST data. These continuum fits were then used to normalize the spectra, together with the photon noise count-rate errors which are propagated through the HST pipeline reduction process along with the flux data.

3. Absorption Line Identification

We first carried out an automatic, objective search for statistically significant absorption fea-

tures in the spectra, using the same absorption-line identification software that has been used for the HST Quasar Absorption Line Key Project, which was kindly made available for us by D. P. Schneider (private communication). The detailed algorithms and line-finding criteria are described fully in Schneider et al. (1993); here we discuss the parameters directly relevant to the current dataset. The line spread functions (LSFs) corresponding to the gratings and apertures used in our FOS and GHRS observations can be characterized approximately by Gaussians with FWHM values as listed in Table 1. These values were used as input for the minimum feature width in the line-finding routine. All the candidate absorption features were fitted with single or, in the case of blends, multiple Gaussian profiles.

In Table 2 we list the final sample of all the absorption features in the HST spectra that have a measured equivalent width W_{obs} greater than or equal to the 3σ detection limit at the wavelength of the line center. We note that at this level, some fraction of the weakest detections might be spurious. Table 2 also gives the 1σ uncertainty in the equivalent width $\sigma(W)$, the significance level of each detection $SL \equiv W_{\text{obs}}/\sigma(W)$, and its measured FWHM value (uncorrected for instrumental broadening). In most cases, a suggested identification is given, together with the redshift if the identified line is extragalactic. All plausible Galactic interstellar medium (ISM) absorption lines were first identified, and we confirmed each of these identifications through a detailed comparison with previously published ISM absorption line studies (e.g., Blades et al. 1988; Bahcall et al. 1991; Savage et al. 1993), as well as transition-strength data tabulated by Morton (1991) and Verner et al. (1994). The remaining lines were identified by assuming each in turn to be an intervening extragalactic Ly α line, and then searching among the other remaining lines for identifications with metal lines or higher-order Lyman lines at the corresponding redshift.

We identify a number of intervening Ly α absorption systems with typical equivalent widths in the range $\sim 0.05 - 0.3 \text{ \AA}$. We note that the two lines at 1251.76 and 1252.46 \AA may at first be taken for high-velocity components of either the Galactic S II $\lambda 1250$ or 1253 lines; however, this is ruled out by the lack of such features in *both* S II lines (which differ only by a factor of 2 in transition strength) as well as in the other, stronger ISM absorption lines. This therefore suggests that these are indeed two Ly α absorption systems, coinci-

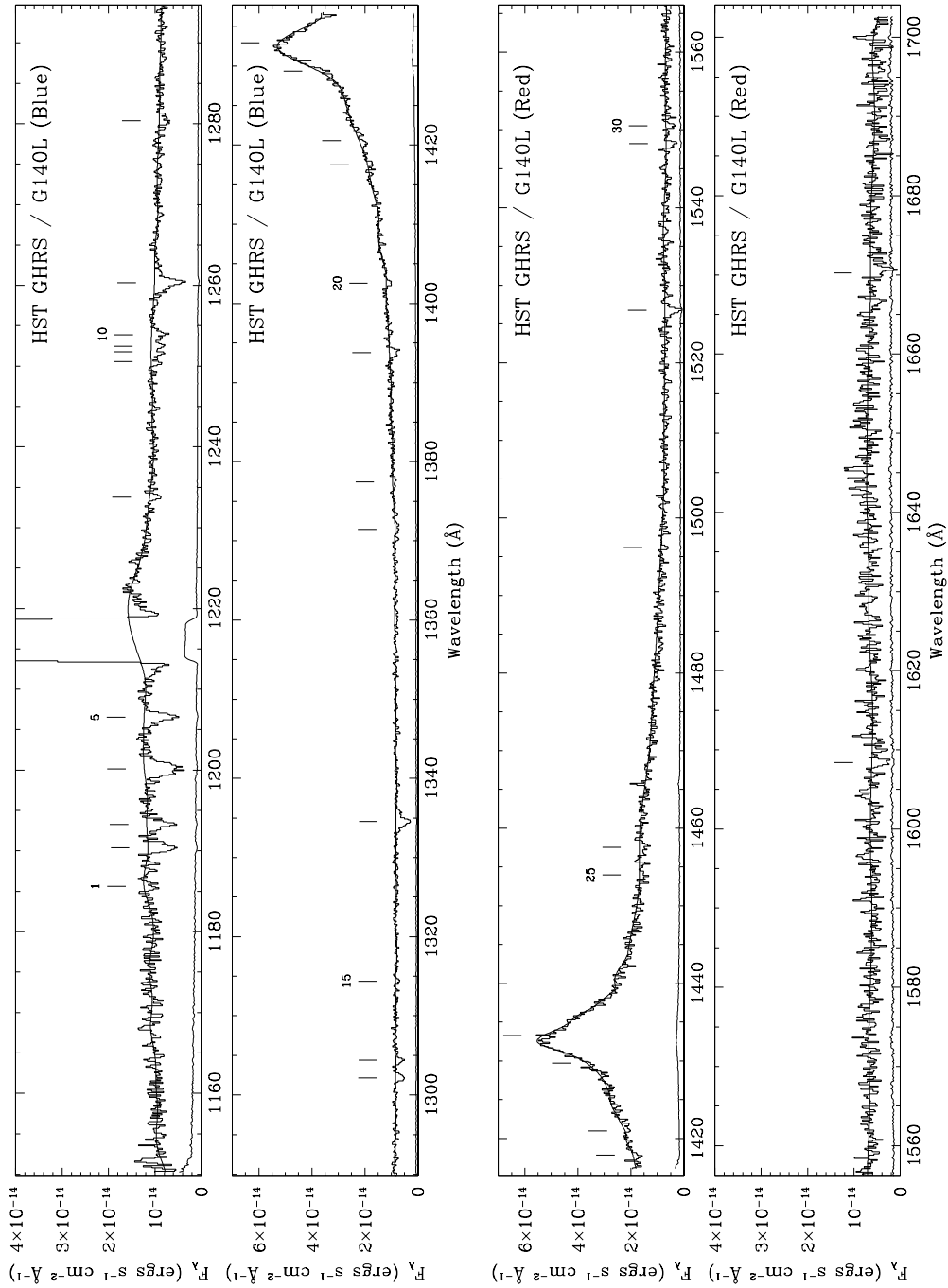


Fig. 1a.— Final calibrated spectra of B2 1028+313, showing each spectral dataset on a separate panel. The flux F_λ in $\text{ergs s}^{-1} \text{cm}^{-2} \text{\AA}^{-1}$ is plotted as a function of wavelength λ . In the HST spectra we also plot the error array derived from the count-rate photon noise, as well as the fitted curve to the “background” emission (continuum plus emission line level) which was used to normalize the spectrum before searching for absorption lines. Vertical bars are used to indicate the positions of all the absorption features detected by the automatic line-finding software, which are tabulated in Table 2. Note also the presence of strong geocoronal Ly α emission at $\sim 1212 - 1220 \text{ \AA}$.

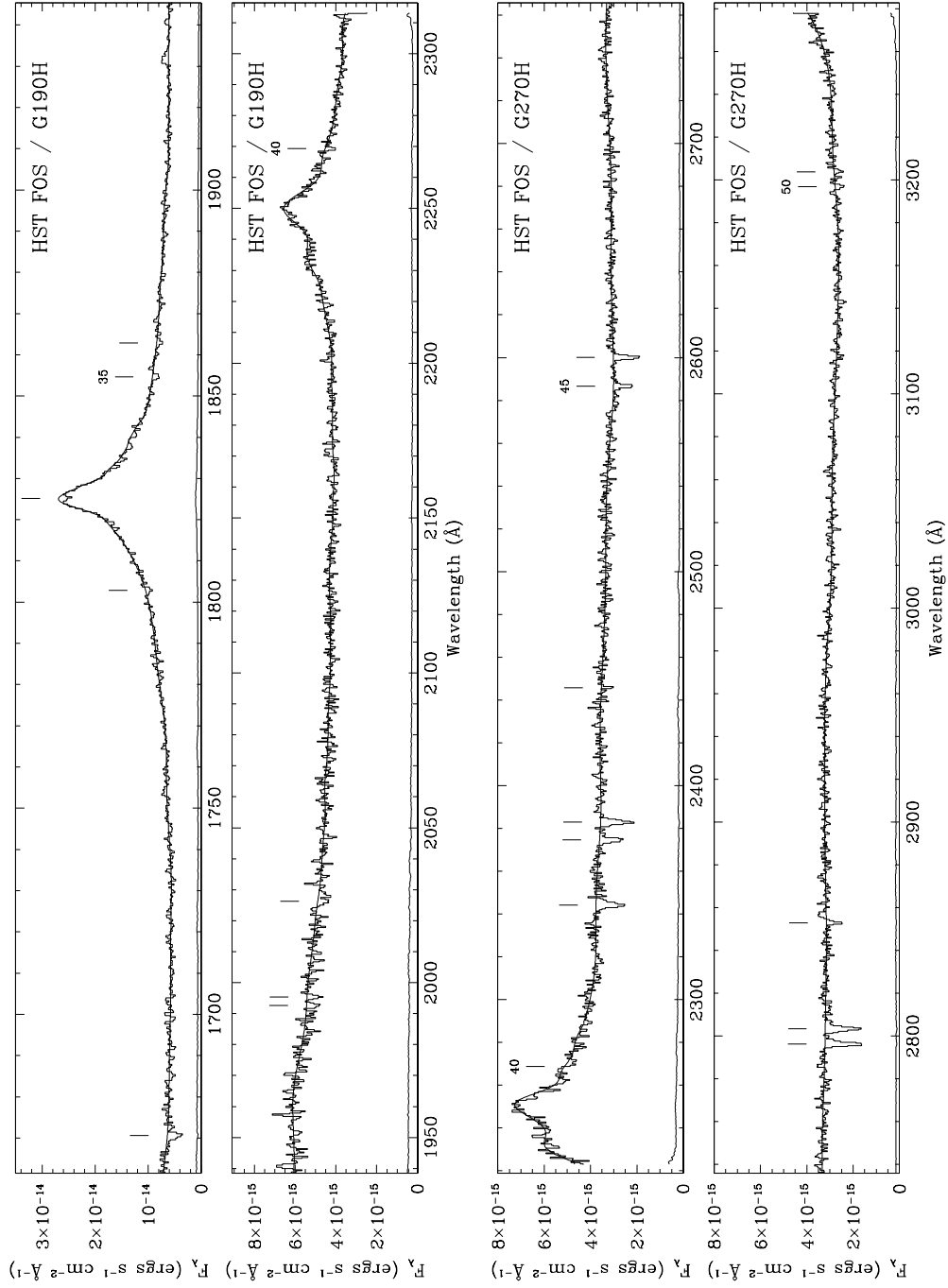


Fig. 1b.— See caption for Fig. 1a

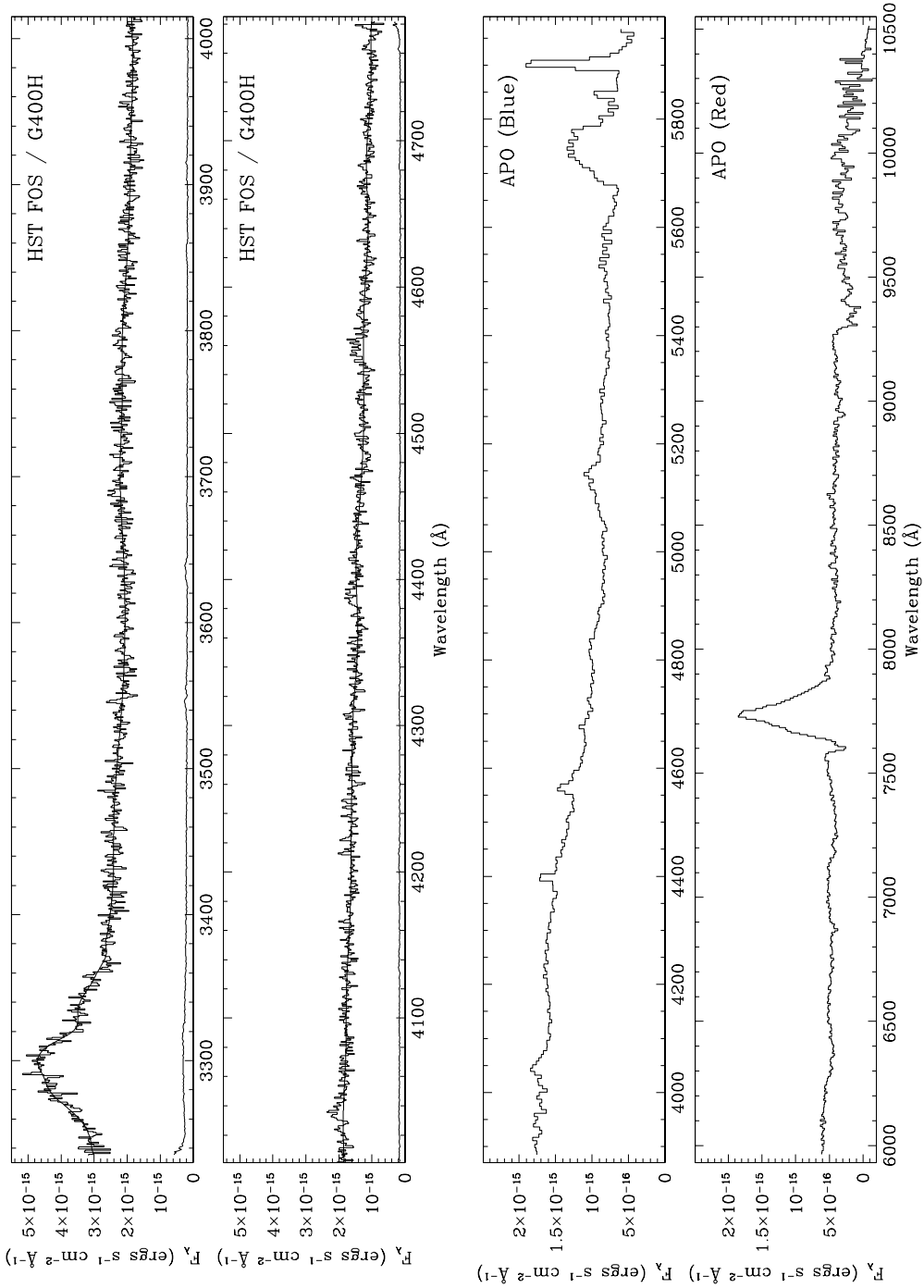


Fig. 1c.— See caption for Fig. 1a

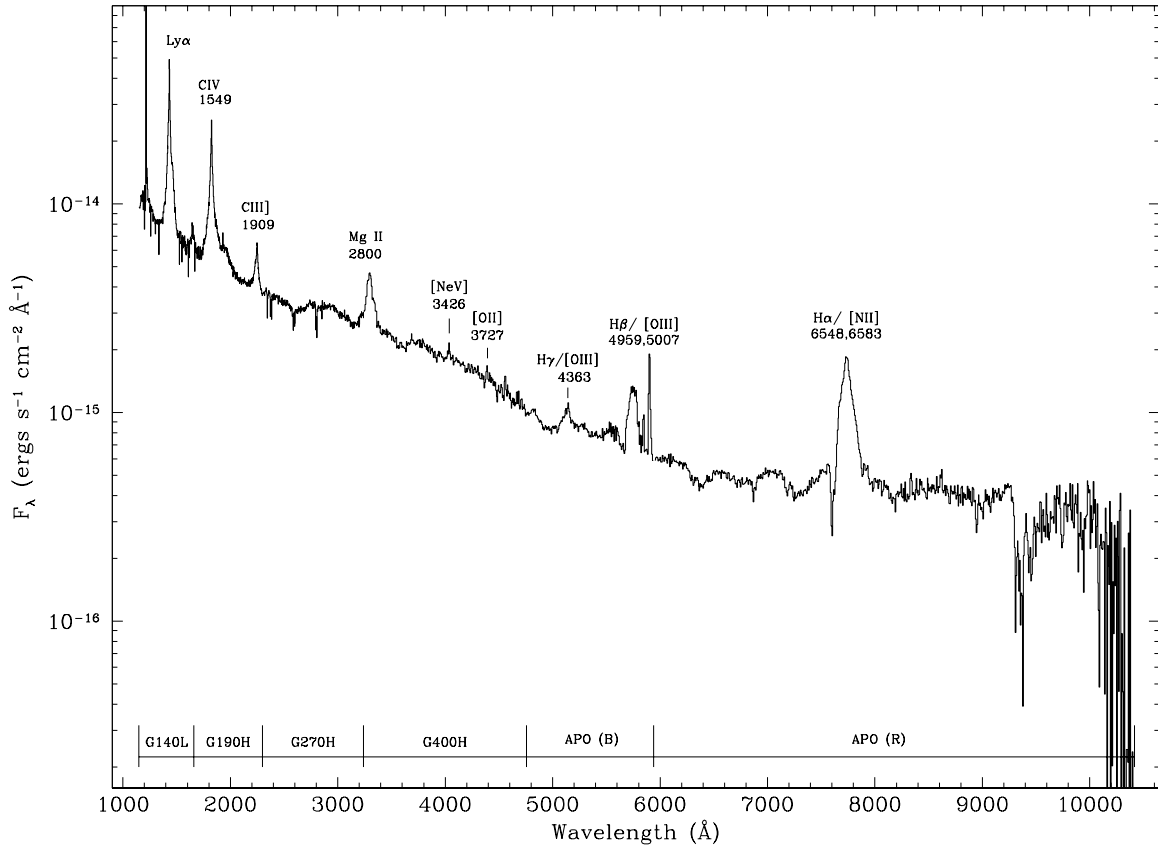


Fig. 2.— Composite spectrum of B2 1028+313, covering the spectral range $\sim 1000 - 10000 \text{ \AA}$. The HST datasets have been binned into intervals $\sim 4 - 6 \text{ \AA}$, in order to provide comparable S/N and spectral resolution to the optical spectra, thereby showing the overall spectral features more clearly.

dentally associated in redshift space with one another and with the Galactic S II absorption lines. Similar identification coincidences have been previously reported in other objects, for example by Bahcall et al. (1993b). We also detect a possible absorption system associated with the quasar redshift, in Ly α and C IV (Figure 3). A more detailed discussion of this system is presented in Appendix A, while in Appendix B we investigate whether or not the apparent C IV associated absorption feature might instead be mimicked by kinematic substructure in the underlying quasar emission-line profile.

4. Search for Absorption Lines from the ICM of Abell 1030

Our primary goal in the present work is to obtain the strongest possible constraints or detection limits on absorption from cold material

that may exist within the ICM of the cluster Abell 1030. The absorption-line identification software described in the previous section can provide some general constraints on the column densities of undetected species. However, these constraints are of limited sensitivity since they are based only on single absorption features. We have developed a powerful and robust technique that allows the limits on all the observable transitions of a given ionic species to be taken into account simultaneously, thereby yielding significantly stronger constraints on its total column density than the limits obtained from a single transition.

We describe here the procedure used in our extensive search for absorption lines from ionized, atomic and molecular gas, which involves obtaining simultaneous constraints on all the observable transitions of each species. From the comprehensive sets of transition-strength and wavelength

data tabulated by Morton (1991) and Verner et al. (1994), we selected all the observable transitions within the wavelength coverage of our HST spectra. We also investigated the possible presence of a number of molecular transitions commonly found in the Galactic ISM (e.g., Van Dishoeck & Black 1986; Black & Van Dishoeck 1987; Morton & Noreau 1994). Our data are of insufficient S/N to allow useful measurements to be obtained from detailed models of the molecular band-head complexes, thus we represent approximate upper limits on absorption from molecular species by the 3σ equivalent width limits derived from the propagated count-rate errors at the relevant locations in the spectrum.

Each selected transition was described in terms of a single Gaussian absorption profile; these were all combined into a template spectrum that was constructed and fitted to the HST spectra by means of the IRAF/STSDAS SPECFIT package (Kriss 1994). The wavelengths of all the transitions were set at fixed ratios relative to one another, thus the entire template was described by a single redshift parameter. The velocity widths of all the transitions were set to be the same (i.e., assuming that any absorption produced by the ICM would display the same kinematic properties in different lines), thus the second parameter describing the template was the velocity dispersion of the absorbing system as a whole. Since we are interested particularly in absorption from the ICM, the velocity dispersions were constrained to lie in the range $\sim 200 - 1000 \text{ km s}^{-1}$ (after accounting for the instrumental profile). Values much narrower than this would more likely be due to absorption from individual objects such as galaxies, while the upper limit of 1000 km s^{-1} corresponds to the largest plausible velocity dispersion for clusters of this richness class (e.g., Fadda et al. 1996). The redshift of the template was allowed to vary by ± 3 times the maximum velocity dispersion (i.e., $\pm 3000 \text{ km s}^{-1}$) relative to the systemic velocity of the quasar, allowing for the detection of possible high-velocity absorption components. Finally, the equivalent widths of all transitions of a given species were fixed relative to the strongest transition, which in turn was allowed to vary freely for each species.

The resulting template contained a total of 486 transitions, typically with about 10–30 transitions for each ionic species. The SPECFIT routine was then used to search the specified parameter space of redshift, linewidth and equivalent width values to fit all the transitions simultaneously, thereby

providing an upper limit on the equivalent width of the strongest transition of each species. The use of large numbers of transitions for each species provides an extremely sensitive means of determining whether or not absorption from a given species is present in the data, particularly when combined with the limited number of free parameters. This method is therefore considerably more robust than using a single transition, and yields a definitive set of constraints on the maximum column density of each species.

The final set of constraints from fitting the template to all the HST spectra are presented in Table 3, where we tabulate the 1σ rest-frame equivalent width limit W_λ , together with the rest wavelength λ_{vac} and oscillator strength f_{ik} of the strongest transition from each species covered by our spectra. The measured equivalent width limits are sufficiently low that the corresponding column densities would be on the linear part of the curve-of-growth for these lines, thus the column density limits N_X are calculated for the limiting case of unsaturated absorption for each tabulated transition. We also note that these limits apply specifically to ICM material, i.e., populations of gas clouds with velocity dispersions in the range $\sim 200 - 1000 \text{ km s}^{-1}$, thus the possible detection of the narrower Ly α and C IV associated absorption lines presented in Table A1 is unrelated to the limits tabulated here.

The limits presented in Table 3 on the column densities of molecular, atomic and ionized species place severe restrictions upon the amount of line-of-sight material with temperatures $T \lesssim 10^6 \text{ K}$. These column density limits are applicable in a general sense to any scenario involving large populations of small clouds in the ICM with a high velocity covering fraction (i.e., displaying a combined velocity profile similar to that of the hot ICM phase). The possibility of significantly higher unobserved column densities can only be accommodated in geometries involving a very small number of cold clouds along the line-of-sight, widely separated in velocity space; or small, very dense clouds with a small area covering factor, containing dust with high extinction. The latter scenario is ruled out in A1030 by the low observed reddening, while analyses carried out by Voit & Donahue (1995) and Braine et al. (1995) for other clusters suggest that X-ray heating should maintain cold gas at temperatures above $\sim 20 \text{ K}$, which is inconsistent with observed radio wavelength molecular absorption limits (O’Dea et al. 1994).

Another possibility is that clouds of cool material may still be present in the cluster, but those along our line-of-sight to the quasar may be ionized by its radiation field and therefore would not be detectable via strong Ly α or molecular absorption. However, it is unlikely that large amounts of gas could be “hidden” in this way, since the expected line luminosity of such clouds at typical ICM pressures and densities (e.g., Voit & Donahue 1995) would be $\sim 3 - 4$ orders of magnitude above the observed upper limit on the H β emission measure (e.m.(H β) $\lesssim 10 - 100$ pc cm $^{-6}$) that is obtained by summing the relevant portion of the long-slit spectrum from Owen et al. (1996).

Thus, it would appear likely that our limits apply generally to gas throughout the ICM of this cluster, in which case we use the observed H I column density upper limit to estimate a constraint on the fraction of neutral gas contributing to the total column density: $N_{\text{H I}}/N_{\text{H}} \lesssim 10^{-8}$, assuming that the column density of X-ray emitting gas is comparable to the values inferred for similar clusters (e.g., David, Jones, & Forman 1995). This rules out the likelihood of a substantial two-phase medium existing in the ICM; instead, the most plausible scenario for the ICM in this cluster is that it exists almost entirely in a hot single phase described by $T \sim 10^7 - 10^8$ K.

5. Conclusions

We have conducted a comprehensive search for UV absorption lines from a possible cool phase of gas that may be present in the ICM of the cluster Abell 1030. The UV-bright quasar B2 1028+313 located at the center of this cluster provides an excellent opportunity to obtain stringent constraints on the existence of any cool component associated with the ICM. The primary result from this study is a comprehensive set of upper limits of $\lesssim 10^{11} - 10^{13}$ cm $^{-2}$ on the column densities of a wide variety of ionized, atomic and molecular species, thereby severely limiting the parameter space of any cool phase ($T \lesssim 10^6$ K) that might possibly be distributed throughout the ICM.

We have also detected possible Ly α and C IV absorption lines from an absorption system apparently associated with the quasar, with an H I column density $\gtrsim 10^{13}$ cm $^{-2}$. The kinematic properties of this system suggest that it may be dynamically associated with the quasar host galaxy, and represents either a companion galaxy / tidal filaments, or otherwise originates in material within $\lesssim 1$ kpc from the AGN.

Our upper limits on the column density of cool material in the ICM apply in a general sense to any scenario involving large populations of small clouds in the ICM with a high velocity covering fraction (i.e., displaying a combined velocity profile similar to that of the hot ICM phase). The possibility of significantly higher unobserved column densities can only be accommodated in geometries involving very few clouds along the line of sight, associated with very cold material ($T \lesssim 10$ K), thus possessing very low velocity covering factors. Otherwise, our results may apply generally to other diffuse (non-cooling flow) clusters: we find that the ICM consists predominantly of a hot phase ($T \gtrsim 10^7$ K), with cool material contributing to $\lesssim 10^{-8}$ of the total column density, thus it is unlikely that significant amounts of the ICM may exist in cooler phases.

Acknowledgements

We would like to thank Tony Keyes and Chris Blades for valuable discussions during the course of this work. We are also very grateful to D. P. Schneider for kindly making available the absorption line identification software package that is used for the HST Quasar Absorption Line Key Project, and for providing vital help regarding the use of this software. We would also like to thank the anonymous referee for useful suggestions that helped to improve the paper. Support for this work was provided by NASA through grant number GO-05934.01-94A from the Space Telescope Science Institute, which is operated by the Association of Universities for Research in Astronomy, Inc., under NASA contract NAS 5-26555. M. Ledlow thanks Elizabeth Rizza for her help in obtaining the APO spectra. The Apache Point Observatory is maintained and operated by the Astrophysical Research Consortium (ARC).

A. The Associated Absorption-Line System

The automatic absorption-line identification software detected absorption features corresponding to Ly α and C IV within ~ 200 km s $^{-1}$ of the systemic velocity of the quasar. We have re-fitted these lines in more detail using the IRAF/STSDAS package SPECFIT (Kriss 1994) and display the resulting best-fit profiles in Figure 3. The C IV profile was fitted using both the $\lambda\lambda 1548, 1550$ Å transitions, and we discuss this line further in Appendix B, where we also consider the possibility

that the apparent C IV absorption might be mimicked by kinematic substructure in the underlying emission profile but demonstrate that this appears improbable, thus in the present discussion we consider this feature to indicate genuine C IV absorption. In Table A1 we tabulate the FWHM and rest-frame equivalent width W_λ of each line, together with its velocity offset ΔV relative to the quasar redshift. We would like to point out that the velocities of the absorption lines are calculated in a frame in which the Galactic ISM absorption lines are at rest, and as such may possibly be offset by up to $\sim 100 - 200 \text{ km s}^{-1}$ from the reference frame in which the quasar redshift was measured by Owen et al. (1995), due to the possible existence of high-velocity Galactic ISM components (e.g., Blades et al. 1988; Savage et al. 1993). Therefore we do not discuss in detail issues concerning infall or outflow of absorbing material with respect to the quasar. The column densities N_X represent lower limits, calculated assuming unsaturated absorption, and the 1σ uncertainties on the parameters are derived from the propagated count-rate errors.

We also detect a weaker Ly α absorption feature with $\Delta V \sim -24 \text{ km s}^{-1}$. This line has a significance level $\sim 2.5 \sigma$, but Figure 4 reveals that it is present in both sections of the overlapping blue and red GHRS G140L spectra, supporting the possibility that it could be a real absorption feature. In this case, the unabsorbed background Ly α emission level should be higher than our interpolated spline fit, and the observed absorption FWHM should be substantially narrower than the instrumental LSF since only the tip of the absorption is observed. This is indeed what we find – the measured FWHM values for both Ly α features are significantly below the 0.87 \AA instrumental resolution. However, the lack of any further quantitative information on the weaker Ly α line precludes a more detailed consideration of its properties, and we limit ourselves to discussing the stronger Ly α and C IV features.

The column density of the Ly α absorption system is $N_{\text{H I}} \gtrsim 10^{13} \text{ cm}^{-2}$ (allowing for the possibility of a higher level of background Ly α emission). This is comparable to the lower end of the column density distribution for Ly α -forest systems in the field (e.g., Honda et al. 1996; Bi & Davidson 1997), which is of interest since this object is in a cluster environment. The relatively narrow linewidth of the absorption, compared with the expected velocity dispersion of the cluster gas, implies that it does not originate in a diffuse col-

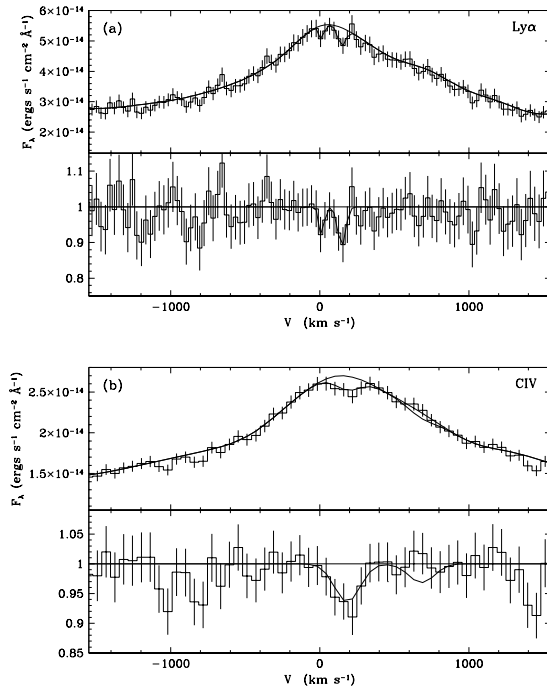


Fig. 3.— The Ly α (a) and C IV (b) absorption systems associated with B2 1028+313. In each case, the upper panel gives the observed spectrum of the emission and absorption lines. The histogram gives the binned observed spectra with $1\text{-}\sigma$ error bars. The thin continuous line is the assumed continuum plus emission line spectrum used to extract the absorption lines. The thicker curve is the best-fit model including the absorption features. In each case, the lower panel displays the residuals after dividing the observed spectrum by the assumed continuum plus emission line spectrum.

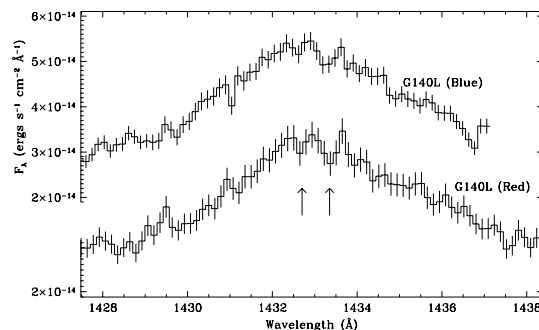


Fig. 4.— Overplot of the two Ly α profiles obtained from the two separate blue and red GHRS/G140L exposures, which overlap in the wavelength range $\sim 1415 - 1436 \text{ \AA}$. The two Ly α absorption features common to both spectra are indicated with arrows.

TABLE A1
ASSOCIATED ABSORPTION-LINE SYSTEM IN ABELL 1030

Line	ΔV (km s ⁻¹)	FWHM ^a (Å)	W_λ (Å)	N_X (cm ⁻²)
Ly α ^b	-24 ± 10	0.19 ± 0.11	0.018 ± 0.007	$3.2 \pm 1.3 \times 10^{12}$
Ly α	110 ± 8	0.30 ± 0.08	0.035 ± 0.008	$6.5 \pm 1.5 \times 10^{12}$
C IV 1548	186 ± 30	1.24 ± 0.41	0.084 ± 0.025	$2.08 \pm 0.62 \times 10^{13}$

^aThe best-fit FWHM values are narrower than the expected instrumental resolution, therefore we do not apply a deconvolution or convert them to velocity space. See text for further details.

^bThis line is below our formal statistical 3 sigma cut-off limit, but as it appears in both overlapping portions of the GHR spectra we have decided to measure and present its properties, as discussed further in the text.

lection of cool clouds in the ICM but rather in a spatially and dynamically coherent object, such as a galaxy or a gas filament. Furthermore, since the systemic velocity of the absorption is so close to that of the quasar (compared to the expected cluster velocity dispersion), it is probably sufficiently close to the quasar to be dynamically associated with it.

One possible origin for the absorption system is a line-of-sight through an intervening cluster galaxy. The relatively small observed H I column may be accounted for if such a galaxy is sufficiently close to the quasar that most of its ISM is ionized as a result of the “proximity effect” (Ellingson et al. 1994), which would also account for the relatively strong C IV absorption. Using the observed spectral energy distribution of the quasar above ~ 10 eV (Elvis et al. 1994; Sarazin et al. 1998), we estimate that an object with a total H column density of 10^{20} cm⁻² and a volume density 1 cm⁻³ can remain ionized by the quasar up to distances of $\sim 50 - 100$ kpc, i.e., sufficiently close to the quasar to also be consistent with a dynamical association.

The low observed column densities may also be produced by tidal debris, which could correspond directly to the extended line-emitting region that has been observed around the quasar by Owen, Ledlow, & Keel (1998). For example, typical gas filaments in such line-emitting regions (spatial scales $\sim 1 - 10$ pc, volume filling factors $\lesssim 10^{-5}$; e.g., Heckman et al. 1989; Morris & Van

Den Bergh 1994) can readily produce the observed column densities. The relatively narrow observed linewidth ($\lesssim 200$ km s⁻¹) is also typical of those generally found in extended emission-line regions associated with luminous active galaxies.

Finally, the associated absorption could be directly related to material within $\lesssim 0.1 - 1$ kpc of the AGN, where the ionization parameter should be sufficiently high to maintain the material at the required ionization state. Such “warm absorbers” have been previously identified in a number of Seyfert galaxies (Turner et al. 1993; Weaver et al. 1994; Reynolds & Fabian 1995; Cappi et al. 1996; Mathur, Wilkes, & Aldcroft 1997). Their inferred H I absorption column densities, together with those of more highly ionized species such as C IV, N V, and O VI, tend to lie in the range $\sim 10^{12} - 10^{14}$ cm⁻² (e.g., Shields & Hamann 1997 and references therein), which compares favorably with our observed Ly α and C IV absorption column densities in Abell 1030. Therefore this is an interesting possibility but difficult to quantify further with our current data, which do not allow good measurements to be obtained of either the N V or O VI absorption lines.

B. Modeling the C IV Profile

A significant dip is evident in the center of the C IV emission-line profile; however, the identification of this as an associated C IV absorption line is complicated by several factors. First, the

emission line may have complex kinematic structures, which can mimic absorption. Second, it is necessary to model both the C IV emission and absorption features as doublets (1548.195, 1550.770 Å), and the fact that the two emission lines are strongly blended by the kinematic structure needs to be taken explicitly into account when considering absorption in the profile. Third, absorption should be seen in both the C IV $\lambda\lambda$ 1548, 1550 absorption lines, with a ratio of transition strengths $R = (f_{ik,2}\lambda_2)/(f_{ik,1}\lambda_1) = 0.5$. The weaker absorption line is not obviously present in Figure 3b. The fit of the C IV $\lambda\lambda$ 1548, 1550 doublet absorption lines is formally consistent with absorption; i.e., the χ^2 value is satisfactory and is indeed decreased by including the absorption lines in the fit, but there is still a slight peak ($\sim 1.5 - 2 - \sigma$) at the expected position of the weaker absorption line.

Thus, there appear to be three possible explanations for the dip in the center of the C IV emission line. First, the entire feature may be a statistical fluctuation, perhaps a combination of low-level instrumental effects and Poisson statistics. We cannot completely rule this out, but consider it quite unlikely. The dip is sampled by ~ 6 pixels and is a statistically significant deviation from even the most conservative interpolated “unabsorbed” profile, and also does not correspond to any known FOS/RD G190H flat-field defect.

Second, the dip might be due to intrinsic structure in the emission line spectrum, either arising from kinematics or from the low-level presence of another species (e.g., Fe II). We see no similar kinematics in the Ly α profile, but this merely shows that either (1) the Ly α and C IV emitting regions are not co-incident in space, or (2) the putative Ly α and C IV absorption is produced by material with different properties. If the spectrum in Figure 3b is due entirely to a complex emission line profile in C IV and there is no absorption, then it should be possible to represent the data as a superposition of the two components of the C IV doublet. We test this by using a deblending algorithm (Hamilton et al. 1997) to separate the two components of the doublet. The total observed flux density $F_{\text{obs}}(v)$ at a velocity v is simply the sum of the two transitions:

$$F_{\text{obs}}(v) = F(v) + RF(v - \Delta v), \quad (\text{B1})$$

where $F(v)$ is the intrinsic profile of the “principal” component having the highest transition strength (1548.195 Å), and $R = (f_{ik,2}\lambda_2)/(f_{ik,1}\lambda_1)$

is the ratio of the intensity of the secondary component (1550.770 Å) relative to the principal component. Provided that the values of Δv and R are known and $R < 1$, equation (B1) can be inverted iteratively to determine the intrinsic C IV λ 1548 profile, $F(v)$, as:

$$\begin{aligned} F_1(v) &= F_{\text{obs}}(v) - RF_{\text{obs}}(v - \Delta v) \\ &\vdots \\ F_{n+1}(v) &= F_n(v) + R^{2n}F_n(v - 2^n\Delta v) \end{aligned} \quad (\text{B2})$$

In practise we found that iterating to $n = 3$ yielded a convergence of $F_n(v) \rightarrow F(v)$ to $\lesssim 1\%$, which is sufficient for these purposes. The primary assumption is that R must be constant for all emitting gas at different velocities (otherwise the two transition profiles would be different shapes). We cannot constrain R independently given our data, thus we assume that R is fixed at 0.5, which is correct if the gas is optically thin and not too dense.

In Figure 5a we present the results of the deblending, carried out for a velocity range ± 4000

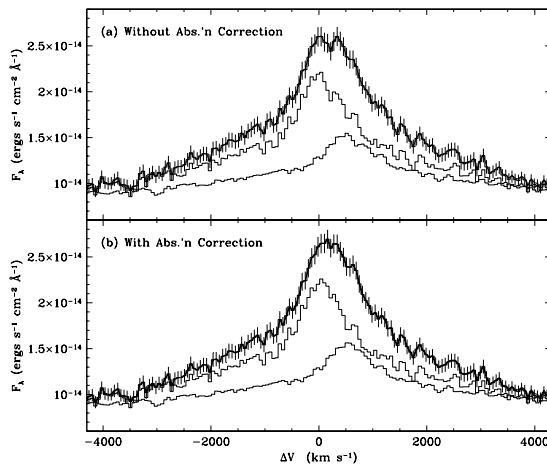


Fig. 5.— The results of deblending the two emission line components of the C IV profile using equation B2. In each panel, the lower thin histograms without error bars give the deblended profiles of the two components at rest wavelengths of 1548.195 Å (left) and 1550.770 Å (right). The upper histogram with error bars is the observed histogram. The upper histogram without error bars is the sum of the two deblended components. (a) The deblending of the emission lines in the observed spectrum without any correction for absorption. (b) The deblending of the emission lines in the observed spectrum after correction for the C IV absorption line doublet as shown in Figure 3b.

km s⁻¹ about the quasar systemic velocity (corresponding approximately to the spectral extent of the C IV emission). The deblended profile is fairly complex, displaying a number of bumps and dips (and similar results are found if the profile is smoothed slightly). However, when the two profiles are overlapped, their dips and bumps anticorrelate, for example at $\sim +500$ km s⁻¹ where an emission peak in the primary component is required to offset a shifted dip in the secondary component. This suggests that the observed feature in the C IV profile cannot be modeled purely by emission-line structure but is intrinsic absorption, and that the other bumps and dips are higher-order “ringing” produced when the deblending algorithm attempts to fit an absorption feature as emission.

Finally, we consider explicitly the hypothesis that the C IV dip indeed arises from an absorption system. One potential difficulty is that the C IV $\lambda 1550$ absorption line is not obviously present in the spectrum. This may be due to an upward statistical fluctuation at that point – the deviation occurs only in 2 pixels, and at the $\sim 1.5\text{-}\sigma$ level. Another possibility is that the secondary absorption line is filled in by the secondary emission line. We have tested this idea by constructing model spectra containing both doublet emission and absorption lines. We find that, while the C IV absorption line strength is partially reduced by the addition of a secondary emission line, this effect is too weak to entirely explain the observed spectra. Another test of the absorption hypothesis is to examine the deblended profiles after correction for the C IV absorption doublet in Figure 3b. These profiles are presented in Figure 5b and are somewhat smoother and less complex than those in Figure 5a, supporting the simpler hypothesis that the absorption is real and not due to complex emission-line kinematics.

Thus, we suggest that the C IV feature represents genuine absorption, and we note that its characteristics are similar to those of other associated C IV absorption systems (Ellingson et al. 1994). However, we caution that our current dataset does not allow us to rule out completely the possibility that it may be mimicked by kinematic substructure in the underlying emission. We have also found this deblending technique to be a powerful means of investigating the underlying profiles of components contributing to a blended observed profile, and recommend its use in studies of associated C IV absorption systems or other cases where the contributing lines are strongly

blended in velocity space.

REFERENCES

- Abell, G. O., Corwin, J., Harold G., & Olowin, R. P. 1989, *ApJS*, 70, 1
- Allen, S. W., Fabian, A. C., Johnstone, R. M., White, D. A., Daines, S. J., Edge, A. C., & Stewart, G. C. 1993, *MNRAS*, 262, 901
- Antonucci, R., & Barvainis, R. 1994, *AJ*, 107, 448
- Bahcall, J. N., et al. 1993a, *ApJS*, 87, 1
- Bahcall, J. N., Jannuzi, B. T., Schneider, D. P., & Hartig, G. F. 1993b, *ApJ*, 405, 491
- Bahcall, J. N., Jannuzi, B. T., Schneider, D. P., Hartig, G. F., Bohlin, R., & Junkkarinen, V. 1991, *ApJ*, 377, L5
- Bi, H., & Davidsen, A. F. 1997, *ApJ*, 479, 523
- Black, J. H., & Van Dishoeck, E. F. 1987, *ApJ*, 322, 412
- Blades, J. C., Wheatley, J. M., Panagia, N., Grewing, M., Pettini, M., & Wamsteker, W. 1988, *ApJ*, 334, 308
- Braine, J., & Dupraz, C. 1994, *A&A*, 283, 407
- Braine, J., Wyrowski, F., Radford, S. J. E., Henkel, C., & Lesch, H. 1995, *A&A*, 293, 315
- Cappi, M., Mihara, T., Matsuoka, M., Hayashida, K., Weaver, K. A., & Otani, C. 1996, *ApJ*, 458, 149
- Cowie, L. L., & Binney, J. 1977, *ApJ*, 215, 723
- Cox, C. V., Bregman, J. N., & Schombert, J. M. 1995, *ApJS*, 99, 405
- David, L. P., Jones, C., & Forman, W. 1995, *ApJ*, 445, 578
- Donahue, M., & Voit, G. M. 1997, in *Galactic and Cluster Cooling Flows*, ed. N. Soker (San Francisco: ASP Press), 48
- Dwarakanath, K. S., Van Gorkom, J. H., & Owen, F. N. 1994, *ApJ*, 432, 469
- Dwek, E., Rephaeli, Y., & Mather, J. C. 1990, *ApJ*, 350, 104
- Edge, A. C., Stewart, G. C., & Fabian, A. C. 1992, *MNRAS*, 258, 177
- Ellingson, E., Yee, H. K. C., Bechtold, J., & Dobrzycki, A. 1994, *AJ*, 107, 1219
- Elvis, M., et al. 1994, *ApJS*, 95, 1
- Fabian, A. C. 1984, in *X-Ray and UV Emission from Active Galactic Nuclei*, ed. W. Brinkmann & J. Trümper (Garching: MPE), 232
- Fabian, A. C. 1994, *ARA&A*, 32, 277
- Fabian, A. C., Nulsen, P. E. J., & Canizares, C. R. 1991, *A&AR*, 2, 191

- Fadda, D., Girardi, M., Giuricin, G., Mardirossian, F., & Mezzetti, M. 1996, *ApJ*, 473, 670
- Francis, P. J., Hewett, P. C., Foltz, C. B., Chaffee, F. H., Weymann, R. J., & Morris, S. L. 1991, *ApJ*, 373, 465
- Hamilton, A. J. S., Fesen, R. A., Wu, C. C., Crenshaw, D. M., & Sarazin, C. L. 1997, *ApJ*, 481, 838
- Heckman, T. M., Baum, S. A., van Breugel, W. J. M., & McCarthy, P. 1989, *ApJ*, 338, 48
- Honda, H., et al. 1996, *ApJ*, 473, L71
- Hu, E. M. 1992, *ApJ*, 391, 608
- Jaffe, W. 1991, *A&A*, 250, 67
- Jaffe, W., & Bremer, M. N. 1997, *MNRAS*, 284, L1
- Kriss, G. 1994, in *Astronomical Data Analysis Software and Systems III*, A.S.P. Conference Series, ed. D. R. Crabtree, R. J. Hanisch, & J. Barnes, 437
- Lazareff, B., Castets, A., Kim, D.-W., & Jura, M. 1989, *ApJ*, 336, L13
- Ledlow, M. J., Loken, C., Burns, J. O., Hill, J. M., & White, R. A. 1996, *AJ*, 112, 388
- Lieu, R., Mittaz, J. P. D., Bowyer, S., Breen, J. O., Lockman, F. J., Murphy, E. M., & Hwang, C. Y. 1996a, *Science*, 274, 1335
- Lieu, R., Mittaz, J. P. D., Bowyer, S., Lockman, F. J., Hwang, C.-Y., & Schmitt, J. H. M. M. 1996b, *ApJ*, 458, L5
- Maoz, D. 1995, *ApJ*, 455, L115
- Mathur, S., Wilkes, B. J., & Aldcroft, T. 1997, *ApJ*, 478, 182
- McNamara, B. R., Bregman, J. N., & O'Connell, R. W. 1990, *ApJ*, 360, 20
- McNamara, B. R., Wise, M., Sarazin, C. L., Januzzi, B. T., & Elston, R. 1996, *ApJ*, 466, L9
- Mittaz, J. P. D., Lieu, R., & Lockman, F. J. 1997, preprint
- Morris, S. L., & Van Den Bergh, S. 1994, *ApJ*, 427, 696
- Morton, D. C. 1991, *ApJS*, 77, 119
- Morton, D. C., & Noreau, L. 1994, *ApJS*, 95, 301
- O'Dea, C. P., & Baum, S. A. 1997, in *Galactic and Cluster Cooling Flows*, ed. N. Soker (San Francisco: ASP Press), 147
- O'Dea, C. P., Baum, S. A., & Gallimore, J. F. 1994, *ApJ*, 436, 669
- O'Dea, C. P., Baum, S. A., Maloney, P. R., Tacconi, L. J., & Sparks, W. B. 1994, *ApJ*, 422, 467
- O'Dea, C. P., Gallimore, J. F., & Baum, S. A. 1995, *AJ*, 109, 26
- O'Dea, C. P., Payne, H. E., & Kocevski, D. 1998, *AJ*, in press
- Owen, F. N., & Ledlow, M. J. 1997, *ApJS*, 108, 41
- Owen, F. N., Ledlow, M. J., & Keel, W. C. 1995, *AJ*, 109, 14
- Owen, F. N., Ledlow, M. J., & Keel, W. C. 1996, *AJ*, 111, 53
- Owen, F. N., Ledlow, M. J., & Keel, W. C. 1998, in preparation
- Owen, F. N., White, R. A., & Ge, J.-P. 1993, *ApJS*, 87, 135
- Rephaeli, Y., & Silk, J. 1995, *ApJ*, 442, 91
- Reynolds, C. S., & Fabian, A. C. 1995, *MNRAS*, 273, 1167
- Sarazin, C. L. 1986, *Rev. Mod. Phys.*, 58, 1
- Sarazin, C. L., Koekemoer, A. M., Baum, S. A., O'Dea, C. P., & Wise, M. W. 1998, *ApJ*, in press
- Sarazin, C. L., & Lieu, R. 1998, *ApJ*, 494, L177
- Savage, B. D., et al. 1993, *ApJ*, 413, 116
- Schneider, D. P., et al. 1993, *ApJS*, 87, 45
- Shields, J. C., & Hamann, F. 1997, *ApJ*, 481, 752
- Soker, N., Bregman, J. N., & Sarazin, C. L. 1991, *ApJ*, 368, 341
- Stickel, M., Lemke, D., Mattila, K., Haikala, L. K., & Haas, M. 1998, *Ann. d'Astrophys.*, 329, 55
- Turner, T. J., Nandra, K., George, I. M., Fabian, A. C., & Pounds, K. A. 1993, *ApJ*, 419, 127
- Van Dishoeck, E. F., & Black, J. H. 1986, *ApJS*, 62, 109
- Verner, D. A., Barthel, P. D., & Tytler, D. 1994, *A&AS*, 108, 287
- Voit, G. M., & Donahue, M. 1995, *ApJ*, 452, 164
- Weaver, K. A., Yaqoob, T., Holt, S. S., Mushotzky, R. F., Matsuoka, M., & Yamauchi, M. 1994, *ApJ*, 436, L27
- White, D. A., Fabian, A. C., Johnstone, R. M., Mushotzky, R. F., & Arnaud, K. A. 1991, *MNRAS*, 252, 72
- Zheng, W., Kriss, G. A., Telfer, R. C., Grimes, J. P., & Davidsen, A. F. 1997, *ApJ*, 475, 469

TABLE 2
ABSORPTION LINES DETECTED TOWARDS ABELL 1030

Line No.	λ_{obs} (Å)	W_{obs} (Å)	$\sigma(W)$ (Å)	SL	FWHM ^a (Å)	Identification; λ_{vac} (Å)	cz_{abs} (km s ⁻¹)
1	1185.60 ± 0.12	0.190	0.056	3.4	0.84 ± 0.29		
2 ^b	1190.40 ± 0.05	0.574	0.055	10.4	1.02 ± 0.12	{ S III 1190.21 Si II 1190.42	48 -5
3	1193.28 ± 0.05	0.527	0.054	9.7	1.02 ± 0.12	Si II 1193.29	-3
4	1200.15 ± 0.05	1.213	0.067	18.09	1.80 ± 0.12	N I 1199.97	45
5	1206.55 ± 0.04	0.683	0.047	14.58	1.14 ± 0.09	Si III 1206.50	12
6	1233.77 ± 0.10	0.170	0.032	5.4	< 0.87	Ly α	4464
7	1250.56 ± 0.09	0.159	0.030	5.4	< 0.87	S II 1250.58	-5
8	1251.76 ± 0.07	0.219	0.029	7.6	< 0.87	Ly α	8900
9	1252.46 ± 0.06	0.236	0.028	8.4	< 0.87	Ly α	9073
10	1253.90 ± 0.06	0.264	0.028	9.5	< 0.87	S II 1253.81	22
11 ^b	1260.32 ± 0.04	0.912	0.046	19.8	1.51 ± 0.09	{ S II 1259.52 Si II 1260.42	190 -24
12	1280.37 ± 0.10	0.266	0.046	5.7	1.19 ± 0.24	Ly α	15955
13	1302.16 ± 0.05	0.366	0.032	11.4	< 0.87	O I 1302.17	-2
14	1304.39 ± 0.06	0.287	0.030	9.5	< 0.87	Si II 1304.37	5
15	1314.37 ± 0.14	0.126	0.033	3.9	< 0.87	Ly α	24340
16	1334.54 ± 0.04	0.921	0.048	19.3	1.44 ± 0.08	C II 1334.53	2
17	1371.43 ± 0.24	0.290	0.067	4.3	2.13 ± 0.57	Ly α	38411
18	1377.43 ± 0.20	0.148	0.049	3.0	1.25 ± 0.48	Ly α	39891
19	1393.80 ± 0.06	0.334	0.041	8.2	1.02 ± 0.15	Si IV 1393.76	9
20	1402.56 ± 0.12	0.140	0.030	4.7	< 0.87	Si IV 1402.77	-45
21	1417.50 ± 0.15	0.098	0.032	3.1	0.91 ± 0.35	Ly α	49773
22	1420.58 ± 0.30	0.169	0.047	3.6	2.19 ± 0.70	Ly α	50532
23	1429.36 ± 0.16	0.070	0.021	3.3	< 0.87	Ly α	52697
24	1432.90 ± 0.09	0.049	0.016	3.1	< 0.87	Ly α	53570
25	1453.98 ± 0.38	0.257	0.086	3.0	2.32 ± 0.91		
26	1457.51 ± 0.17	0.223	0.063	3.5	1.25 ± 0.41		
27	1496.16 ± 0.17	0.208	0.062	3.4	< 0.87		
28	1526.74 ± 0.04	0.820	0.080	10.2	0.89 ± 0.10	Si II 1526.71	6
29	1548.20 ± 0.09	0.449	0.074	6.1	< 0.87	C IV 1548.20	0
30	1550.52 ± 0.12	0.358	0.078	4.6	< 0.87	C IV 1550.77	-48
31	1608.42 ± 0.09	0.566	0.131	4.3	0.84 ± 0.24	Fe II 1608.45	-6
32	1670.59 ± 0.11	0.728	0.103	7.0	1.61 ± 0.27	Al II 1670.79	-36
33 ^c	1802.84 ± 0.26	0.158	0.046	3.5	< 1.47		
34	1825.16 ± 0.22	0.112	0.028	4.1	< 1.47	C IV 1548.20	53630
35	1854.67 ± 0.16	0.199	0.052	3.9	1.24 ± 0.38	Al III 1854.72	-8
36	1862.89 ± 0.21	0.191	0.058	3.3	1.41 ± 0.49	Al III 1862.79	16
37	1992.59 ± 0.25	0.186	0.051	3.6	< 1.47		
38	1995.36 ± 0.25	0.188	0.052	3.6	< 1.47		
39	2026.34 ± 0.25	0.199	0.057	3.5	< 1.47	{ Zn II 2026.14 Mg I 2026.48	30 -21
40	2269.34 ± 0.28	0.140	0.043	3.2	< 1.47		
41	2344.25 ± 0.14	0.976	0.096	10.1	2.86 ± 0.33	Fe II 2344.21	5

TABLE 2—*Continued*

Line No.	λ_{obs} (Å)	W_{obs} (Å)	$\sigma(W)$ (Å)	SL	FWHM ^a (Å)	Identification; λ_{vac} (Å)	cz_{abs} (km s ⁻¹)
42	2374.62 ± 0.14	0.691	0.086	8.0	2.24 ± 0.33	Fe II 2374.46	20
43	2382.89 ± 0.09	0.928	0.080	11.5	2.22 ± 0.22	Fe II 2382.77	15
44 ^d	2445.65 ± 0.42	0.214	0.069	3.1	< 2.04		
45	2586.66 ± 0.14	0.597	0.061	9.8	< 2.04	Fe II 2586.65	1
46	2600.13 ± 0.10	0.812	0.054	15.2	< 2.04	Fe II 2600.17	-5
47	2796.24 ± 0.05	1.144	0.063	18.1	2.06 ± 0.13	Mg II 2796.35	-12
48	2803.35 ± 0.06	1.182	0.067	17.7	2.30 ± 0.15	Mg II 2803.53	-19
49	2852.82 ± 0.18	0.409	0.055	7.5	< 2.04	Mg I 2852.96	-15
50	3196.83 ± 0.28	0.267	0.058	4.6	< 2.04		
51	3203.89 ± 0.30	0.246	0.059	4.2	< 2.04		

^aThe FWHM values are those measured directly, uncorrected for instrumental broadening. Completely unresolved lines are indicated as upper limits.

^bAt these wavelengths, both S and Si lines are usually identified (e.g., Blades et al. 1988; Bahcall et al. 1993a; Savage et al. 1993); however we note that the S transition strengths for these lines are $\sim 1 - 2$ orders of magnitude weaker than those of Si.

^cBased on the detected Ly α redshifts along the line of sight, the only strong candidate identification is Si II $\lambda 1526$ at $z = 0.1799$. However, there is no significant detection of the stronger Si II $\lambda\lambda 1190, 1193$ transitions at the same redshift, therefore we regard this identification as spurious.

^dBased on the detected Ly α redshifts along the line of sight, the only strong candidate identification is Fe II $\lambda 2374$ at $z = 0.0296$. However, the lack of the stronger Fe II $\lambda\lambda 2344, 2383$ transitions at the same redshift makes this identification unlikely.

TABLE 3
UPPER LIMITS ON ICM ABSORPTION COLUMN DENSITIES

Species	λ_{vac} (Å)	f_{ik}	$1-\sigma W_\lambda$ (Å)	$1-\sigma \log N_X$ (cm^{-2})
H I	1215.7	0.4164	0.013	12.4
C I	1656.9	0.1404	0.045	13.1
C II	1334.5	0.1278	0.012	12.8
C III	977.0	0.7621	0.022	12.5
C IV	1548.2	0.1908	0.019	12.7
N I	1200.0	0.2655	0.020	12.8
N II	1084.0	0.1031	0.055	13.7
N III	989.8	0.1066	0.027	13.5
N V	1238.8	0.1570	0.013	12.8
O I	1302.2	0.0489	0.021	13.5
Mg I	2853.0	1.8304	0.037	11.4
Mg II	2796.4	0.6123	0.015	11.5
Al I	1765.6	0.5769	0.024	12.2
Al II	1670.8	1.8330	0.053	12.1
Al III	1854.7	0.5602	0.028	12.2
Si I	1562.0	0.3758	0.026	12.5
Si II	1260.4	1.0072	0.047	12.5
Si III	1206.5	1.6694	0.038	12.2
Si IV	1393.8	0.5140	0.048	12.7
P I	1774.9	0.1543	0.010	12.4
P II	1152.8	0.2361	0.013	12.7
P III	998.0	0.1117	0.045	13.7
P V	1118.0	0.4732	0.030	12.8
S I	1425.0	0.1918	0.049	13.2
S II	1259.5	0.0162	0.016	13.8
S III	1190.2	0.0222	0.021	13.9
S IV	1062.7	0.0400	0.015	13.6
Cl I	1004.7	0.1577	0.062	13.6
Cl II	1071.0	0.0150	0.018	14.1
Cl III	1015.0	0.0213	0.021	14.0
Ar I	1048.2	0.2441	0.018	12.9
Ca I	2276.2	0.0701	0.019	12.8
Ca II	3934.8	0.6346	0.021	11.4
Cr I	3579.7	0.3664	0.054	12.1
Cr II	2056.3	0.1403	0.057	13.0
Cr III	1040.1	0.1222	0.052	13.6
Fe I	2484.0	0.5569	0.035	12.1
Fe II	2600.2	0.2239	0.013	12.0
Fe III	1122.5	0.0788	0.053	13.8
Ni I	2320.7	0.6851	0.027	11.9
Ni II	1741.5	0.1035	0.041	13.2
Zn I	2139.2	1.4593	0.048	11.9
Zn II	2062.7	0.2529	0.053	12.7
H ₂	986.0	0.1300	0.013	13.1
HD	1011.0	0.0244	0.021	13.9

TABLE 3—*Continued*

Species	λ_{vac} (\AA)	f_{ik}	$1-\sigma W_\lambda$ (\AA)	$1-\sigma \log N_X$ (cm^{-2})
C ₂	1342.0	0.1000	0.018	13.1
CO	1089.0	0.1630	0.057	13.5
OH	1222.0	0.1000	0.038	13.5
H ₂ O	1240.0	0.1500	0.058	13.4
O ₂	1820.0	0.0300	0.052	13.8
SiO	1310.0	0.1000	0.060	13.6